REPORT DOCUMENTATION PAGE

AFRL-SR-AR-TR-08-0284

1. REPORT DATE *(DD-MM-YYYY)*	2. REPORT TYPE	3. DATES COVERED *(From - To)*
14-05-2008	Final Report	2/15/07 - 2/14/08

4. TITLE AND SUBTITLE

Pre-Flight Ground Testing of the Full-Scale HIFiRE-1 at Fully Duplicated Flight Conditions

5a. CONTRACT NUMBER

5b. GRANT NUMBER

FA9550-07-1-0150

5c. PROGRAM ELEMENT NUMBER

6. AUTHOR(S)

Wadhams, Tim, P.
MacLean, Matthew, G.
Holden, Michael, S.
Mundy, Erik

5d. PROJECT NUMBER

5e. TASK NUMBER

5f. WORK UNIT NUMBER

7. PERFORMING ORGANIZATION NAME(S) AND ADDRESS(ES)

CUBRC, Inc.
4455 Genesee Street
Buffalo, NY 14225

8. PERFORMING ORGANIZATION REPORT NUMBER

9. SPONSORING/MONITORING AGENCY NAME(S) AND ADDRESS(ES)

AF OFFICE OF SCIENTIFIC RESEARCH
875 N. RANDOLPH ST. ROOM 3112
ARLINGTON VA 22203
Dr John Schmisseur/NA

10. SPONSOR/MONITOR'S ACRONYM(S)

AFRL, AFOSR

11. SPONSOR/MONITOR'S REPORT NUMBER(S)

12. DISTRIBUTION/AVAILABILITY STATEMENT

Approved for public release; distribution is unlimited.

13. SUPPLEMENTARY NOTES

14. ABSTRACT

As part of an experimental study to obtain detailed heating and pressure data over the full-scale HIFiRE-1 flight geometry, CUBRC has completed a 30-run matrix of ground tests, sponsored by the AFOSR, to determine the optimal flight hardware and instrumentation configuration necessary to achieve and make measurements of desired flow phenomena during the flight experiment HIFiRE-1 stands for Hypersonic International Flight Research and Experimentation and the flight vehicle consists of a blunt nose, cone, cylinder, and flare regions. The primary objective of the HIFiRE-1 flight experiment is to collect high quality flight data to be used for CFD code and ground test facility validation in regions of boundary layer transition as well as regions of separated shock wave/boundary layer interaction at the cylinder/flare junction.

15. SUBJECT TERMS

HIFiRE-1, Flight Experiment, Boundary Layer Transition, Turbulent Shock/Boundary Layer Interaction

16. SECURITY CLASSIFICATION OF:			17. LIMITATION OF ABSTRACT	18. NUMBER OF PAGES	19a. NAME OF RESPONSIBLE PERSON
a. REPORT	b. ABSTRACT	c. THIS PAGE			Timothy P. Wadhams
Unclassified	Unclassified	Unclassified	UU	23	19b. TELEPHONE NUMBER *(Include area code)* 716-204-5125

Pre-Flight Ground Testing of the Full-Scale HIFiRE-1 at Fully Duplicated Flight Conditions

T.P. Wadhams*, M.G. MacLean†,
M.S. Holden‡, E. Mundy§
CUBRC, Buffalo, New York 14225

Abstract

As part of an experimental study to obtain detailed heating and pressure data over the full-scale HIFiRE-1 flight geometry, CUBRC has completed a 30-run matrix of ground tests, sponsored by the AFOSR, to determine the optimal flight hardware and instrumentation configuration necessary to achieve and make measurements of desired flow phenomena during the flight experiment HIFiRE-1 stands for Hypersonic International Flight Research and Experimentation and the flight vehicle consists of a blunt nose, cone, cylinder, and flare regions. The primary objective of the HIFiRE-1 flight experiment is to collect high quality flight data to be used for CFD code and ground test facility validation in regions of boundary layer transition as well as regions of separated shock wave/boundary layer interaction at the cylinder/flare junction. While flight data will be acquired over the entire flight, data was obtained in LENS I over a range of Mach numbers from 6.5 to 7.4, and Reynolds numbers of 2E+06 to 5.5E+6 duplicating the reentry trajectory points that gave the best chance to measure the transition process on the cone and have a turbulent separated flow that reattached onto the flare section. These test condition ranges were determined directly from the nominal descent trajectory of the Australian Terrier-Orion launch vehicle that would serve as the booster for HIFiRE-1. The program was completed in two distinct phases. The first phase consisted of a geometry study to aid in the selection of the proper nose radius to achieve the desired transition location on the cone, and to establish the flare angle necessary to achieve a turbulent separation zone with reattachment back onto the flare. These experimental results were used directly in determining the proper nose radius to employ for both the second phase of the ground test and for use on the actual flight vehicle and to determine where additional instrumentation should be placed to obtain higher resolution spatially in the transition region. These areas included the transitional region on the cone as the flow goes from fully laminar to fully turbulent, and at the cylinder/flare junction to obtain detailed information in the shock wave/turbulent boundary layer region with separation and reattachment. Additionally high speed schlieren movies were taken during the first phase to assess the separation behavior in the cylinder/flare region. It was very desirable to achieve turbulent separation with reattachment on the flare far enough upstream to leave an attached length on the flare after reattachment to serve as a bounding condition for CFD validation. Secondary objectives of the first phase included testing the model at angle of attack and heating the model nose to flight-like temperatures to assess the influence of these factors on the transition front and separation/reattachment process. In addition to the experimental data, CUBRC also performed a large amount of CFD analysis to confirm and validate not only the tunnel flow conditions, but also 2D and 3D flows over the model itself. Laminar and turbulent solutions have been obtained using the DPLR code, including several distinct turbulence models. This analysis is a standard part of any experimental program at CUBRC, and this information was of key importance for post-test data quality analysis (correlation) and understanding particular phenomena seen in the data. A key part of the computational study involved establishing "n-factors" to compare DPLR and STABL transition results to those obtained in the experiment. These comparisons were ultimately employed to extrapolate the transition location to flight. All work during this effort was sponsored by AFOSR.

---

* Research Scientist, AAEC, CUBRC, 4455 Genesee Street, Buffalo, NY, Member.
† Senior Research Scientist, AAEC, CUBRC, 4455 Genesee Street, Buffalo, NY, Member.
‡ Program Manager, AAEC, CUBRC, 4455 Genesee Street, Buffalo, NY, Fellow.
§ Research Scientist, AAEC, CUBRC, 4455 Genesee Street, Buffalo, NY, Member.
Experimental work and analysis performed during this program was supported and directed under contract to the Air Force Office of Scientific Research (AFOSR)

I. Introduction and Program Overview

Over the past year, experimental and computational studies have been conducted by CUBRC to assist in the selection of a blunted cone/cylinder/flare configuration to be employed in the AFOSR-sponsored HIFiRE-1 flight test program to be conducted by the Australian HIFiRE team. HIFiRE-1 stands for Hypersonic International Flight Research and Experimentation and the objective of the ground test program was to select the nosetip and flare configurations which would provide the most useful sets of boundary layer transition data on the cone, and regions of fully turbulent shock wave/boundary layer interaction with a separation length which would provide key information with which to evaluate the prediction methods to describe regions of shock wave/turbulent boundary layer interaction in hypersonic flows. CUBRC's LENS I hypervelocity shock tunnel was selected to meet these objectives because of the facility's capability to duplicate the required freestream conditions while testing a full-scale version of the flight vehicle. Freestream conditions for these studies were selected from the trajectory of the Australian Terrier-Orion booster, the launch vehicle for the flight test, at points where transition would occur in a desirable location on the cone. Angle of attack measurements were also obtained as they pertain to the expected trajectory to explore the three-dimensional transition and shock/wave turbulent boundary layer interaction effects the vehicle will experience in flight. Additionally high-speed schlieren movies were taken of the flare region to assess separated region length for variations in flare angle, freestream condition, and model attitude. The flare was not initially instrumented to allow the experimenters to easily change the angle with minimal downtime between runs. The experimental results will be applied directly to the design geometry of the flight vehicle and be compared against computational results and the eventual flight data. The data will also be used to guide the placement of additional instrumentation in both the transition and shock interaction regions for the second phase of ground test program. In parallel with the experimental study CUBRC preformed a large amount of computational work assessing both the flow in the test facility and the freestream flow over the model. These computational results include laminar and turbulent predictions of pressure and heat transfer on the cone and cylinder sections employing the DPLR code, and stability calculations of the forebody utilizing STABL. The laminar calculations were an important confirmation of the experimental results and flow conditions and as validation of the computational results that would be directly applied to the stability calculations. The turbulent calculations will be used to assess how well various turbulence modeling techniques are able to accurately predict these flows. Finally employing the STABL "n-factor" results flight transition location estimates were made and compared to ground test results. A follow-up program is currently underway with additional instrumentation located in the transition region and a fully instrumented flare to fully detail both the transition process and the shock/wave turbulent boundary layer interaction in the cylinder flare region. Additional goals in the second phase will include tripping studies, further angle of attack test points, and an assessment of the second mode transition frequencies on the cone section of the model.

II. Facilities and Instrumentation

A. The LENS Facility

The aerothermal tests in this program were performed in the LENS I hypervelocity reflected shock tunnel. A schematic diagram of the LENS I HST is shown alongside the LENS II and LENS X facilities in Figure 1. The three facilities share a common control system, compressor system, data recording system and data analysis system. LENS I has the capability to fully duplicate flight conditions at Mach numbers ranging from 6 to 15, while LENS II has similar capabilities from Mach 3 to 7. The major components of the LENS I facility include a 25.5-foot long by 11-inch diameter electrically heated driver tube, a double diaphragm assembly, a 60-foot by 8-inch diameter driven tube, a fast acting centerbody valve assembly, multiple nozzles to achieve desired test conditions from Mach 6 to 18, and a test section capable of accommodating models up to 3 feet in diameter and 12 feet long. A new nozzle upgrade will soon take this capability up to Mach 22. The LENS II facility is similar in construction, incorporating 24-inch driver and driven tubes that are 60- and 100-feet in length respectively and is currently capable of running between Mach 3 and 7. Upgrades are underway to increase the performance to Mach 10. The LENS II facility is capable of test times between 100 and 20 msec at

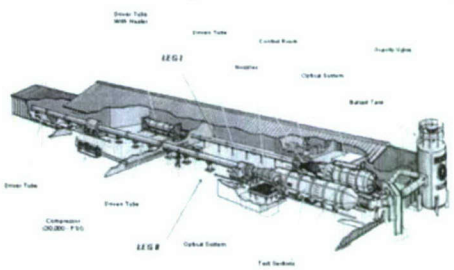

Figure 1. Schematic Drawing of the LENS I and LENS II Hypersonic Shock Tunnel Facilities and LENS X Expansion Tunnel

velocities from 3,000 to 8,000 ft/sec respectively. The LENS X facility is a large expansion tunnel which is assembled with major components from the LENS II facility together with new diaphragm stations and tube components. This tunnel shares compressors, vacuum pumps, and the data system with the other LENS tunnels.

The high-pressure driver section of LENS I has the capacity to operate at 30,000 lb/in^2 using heated driver gases of hydrogen, helium, nitrogen or any combination of the three. The driver gases can be heated up to 750°F and the amount of each gas varied to achieve tailored interface operations for maximum test times. The driven tubes of either facility can use air, nitrogen, carbon dioxide, helium, hydrogen or any other gases or combinations of gases for model testing.

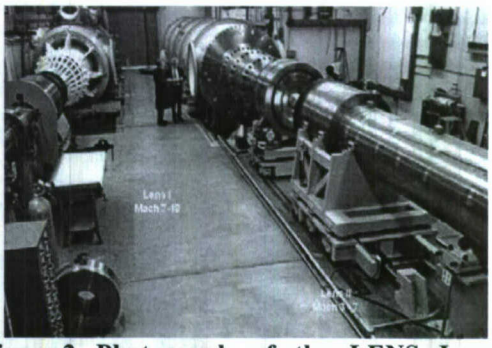

Figure 2. Photograph of the LENS I and LENS II Facilities at the Aerothermal Aero-Optics Evaluation Center

A schematic diagram illustrating the basic operation of the shock tunnel is shown in Figure 3. Both LENS I and LENS II tunnels operate with tailored interface conditions to maximize test condition uniformity and run time. Tailored conditions are achieved by carefully controlling the pressures and gas mixtures used in the driver and driven tubes of the tunnel to achieve a condition where the contact surface between driver and driven gases is transparent to the reflected shock. Flow is initiated through the tunnel by rapidly pressurizing the center section of the double diaphragm unit causing the diaphragms to rupture. The sudden release of the driver gas generates a strong shock which travels down the driven tube, is reflected from the end wall, and travels back up the driven tube, creating a stagnant, high-pressure, high-temperature reservoir of test gas. When the reflected shock strikes the interface in its return path, the condition in the driver and driven tubes are controlled such that the contact surface is brought to rest. The reservoir of hot stationary test gas between the end wall and the contact surface is exhausted through the throat section of the nozzle into the test section in a manner similar to any blowdown tunnel. The flow through the nozzle is terminated when a fast-acting valve closes the throat section.

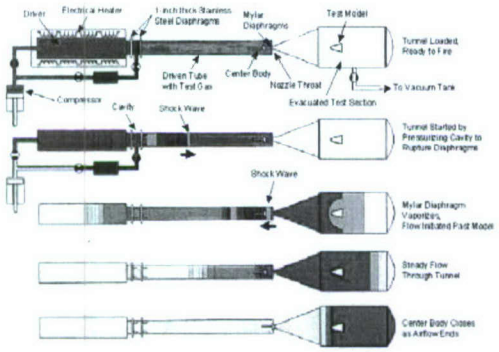

Figure 3. Basic Operation of LENS Facilities

A velocity/altitude map for the LENS facilities is shown in Figure 4. This map includes the ascent and descent trajectories of the Australian Terrier-Orion launch vehicle that will serve as the booster for HIFIRE-1. The stars represent the test points of interest in this study. By operating the LENS tunnel under cold conditions (just above the liquefaction temperature of the airflow in the test section), large Reynolds numbers and test times can be obtained in the LENS I facility for studies where only Mach number, Reynolds number simulation is required. A Reynolds number and Mach number performance plot for the LENS facility, again including the HIFIRE-1 trajectory, is shown in Figure 5. A complete listing of LENS facility capabilities is shown in table form in Figure 6 and can be found in the references [AAEC Staff 2004].

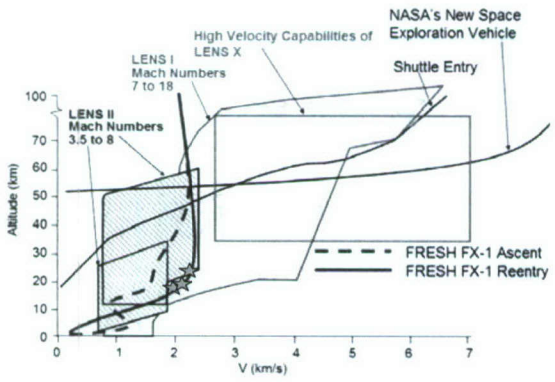

Figure 4. LENS Facility Altitude Velocity Map

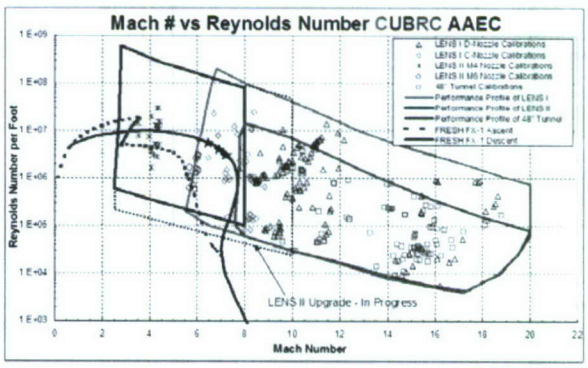

Figure 5. Mach Number/Reynolds Number Envelope

LENS I
Velocity Range (ft/sec)
3,000 – 15,000
Altitude (kft)
25 - 300
Mach Numbers
8.0 - 18.0
Reynolds Numbers (1/ft)
1.0E4 - 1.0E8
Test Time (ms)
up to 25
Nozzles
Mach 8 – 10 (48" Exit)
Mach 10 – 18 (48" Exit)

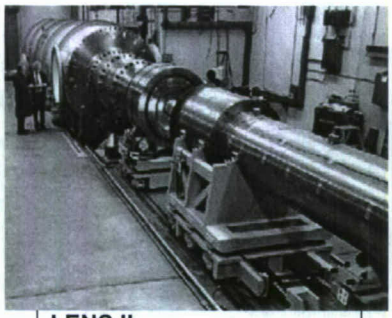

LENS II
Velocity Range (ft/sec)
2,500 – 9,000
Altitude (kft)
SL - 200
Mach Numbers
3.0 - 10.0
Reynolds Numbers (1/ft)
1.0E5 - 1.0E9
Test Time (ms)
up to 100
Nozzles
Mach 3 – 5 (42" Exit)
Mach 5 – 8 (60" Exit)

LENS X
Velocity Range (ft/sec)
14,000 – 22,000
Altitude (kft)
120 - 250
Mach Numbers
14.0 - 22.0
Reynolds Numbers (1/ft)
1.0E3 - 1.0E6
Test Time (ms)
up to 4
Nozzles
Mach 14 – 22 (60" Exit)

Figure 6 Operational Range of LENS Facilities

B. Heat Transfer Instrumentation

For these studies we primarily employed platinum thin-film heat transfer instrumentation similar to those designed at Cornell Aeronautical Laboratory (CAL) in the late 1950s and refined over the past 50 years. The platinum thin-film heat transfer instrumentation employed in these studies have proven to be the most accurate measurement technique in supersonic and hypersonic test facilities, and the small size of the sensing element coupled with the insulating substrate make them ideal for measuring a high resolution level and location of the heating on the surface of the model. CUBRC has calculated the accuracy of the heat transfer measurement to be ±5%.

Figure 7a. 0.125" Thin-film Heat Transfer Instrument

Figure 7b. 0.040" Thin-film Heat Transfer Instrument

The thin-film heat transfer gauge is a resistance thermometer that measures the local surface temperature of the model. The theory of heat conduction is used to relate the surface temperature history to the rate of heat transfer. Since the platinum resistance element has negligible heat capacity, and hence negligible effect on the Pyrex surface temperature, the gauge can be characterized as being homogeneous and isotropic with properties corresponding to those of the Pyrex. Furthermore, because of the short duration of shock tunnel tests, the Pyrex can be treated as a semi-infinite body. Examples of the types of thin-film instrumentation employed in this test can be seen in Figures 7-8. Because of the requirement to obtain transitional data in this program all the thin-film sensors needed to be specially matched and contoured to the surface of the model. Using very small sensors (Figure 7b) on the cone section (Figure 8) greatly helped to achieve an acceptably smooth model. There is the potential to obtain erroneous transition data from any misaligned sensors tripping or disturbing the flow.

The platinum thin-film sensor, with a frequency response over 300 kHz, is also ideal in obtaining fluctuating heat transfer levels. This information is important to define the transitional flow characteristics on the model. If an adequate amount of sensors are placed in the transition zone the transition process can be accurately followed from the initial disturbances, to the turbulent bursts, to the fully turbulent levels. Typically transition is viewed as occurring at a particular geometric point, but in real life the transition front can be described as moving

forward and backward over time. The thin-film sensor is the most accurate method to describe the limits of the movement and the associated heating rates.

It was determined that a total of 50 platinum thin-film sensors, distributed along the length of the model and at 0, 90, 180, and 270 degrees around the model, would be needed to evaluate the cone transition, assess when the flow became fully turbulent on the cone, and if it remained turbulent after it had passed onto the cylinder. This number will be increased dramatically in the next phase of the program once the desired transition location and the optimal flare angle have been established.

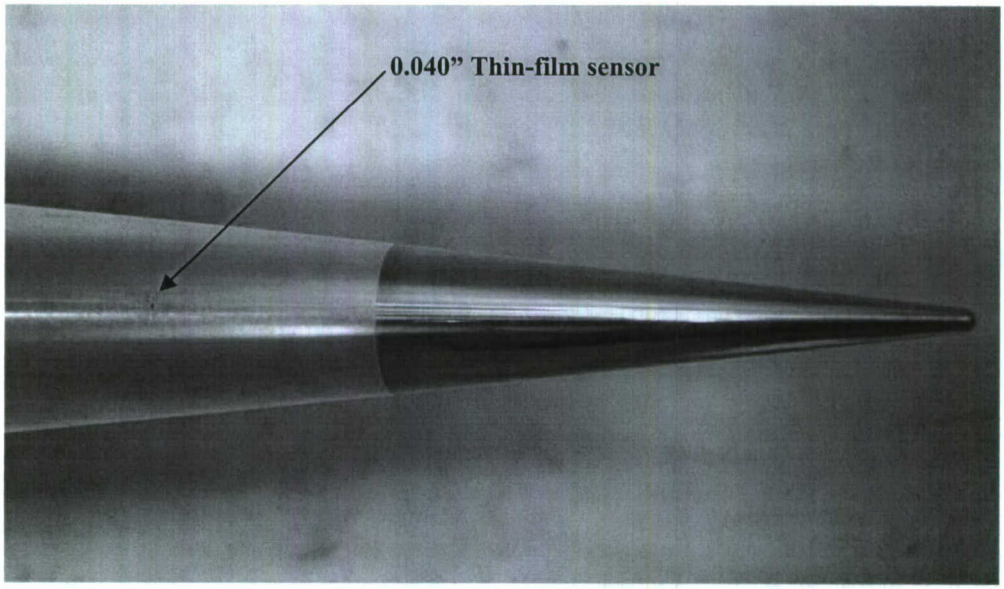

Figure 8. 0.04" Thin-film Sensors Placed in FRESH FX-1 Nose Cone

C. Pressure Instrumentation

For these studies, we primarily employed piezoelectric pressure gauge instrumentation that, like the platinum thin-film sensor, was originally designed at Cornell Aeronautical Laboratory. These gauges employ a diaphragm design and read the model pressure versus a pretest baseline pressure (differential pressure). In the data reduction process this baseline, or pre-run pressure, is subtracted off the final measurement to yield an absolute measurement. Additionally, these transducers are mounted close to the surface of the test article so that orifice effects and fill times are negligible. The piezoelectric pressure transducers, manufactured by PCB, are capable of accurately measuring pressures within ±3%. Figure 9 shows a typical PCB piezoelectric pressure transducer.

Where size constraints do not allow for PCB style instrumentation CUBRC employs both Endevco and Kulite piezoresistive type transducers. These transducers have a very small sensing footprint and can be installed in difficult geometry locations. These sensors also typically have a higher frequency response (~100 kHz) than the standard piezoelectric sensors we employ. The piezoresistive strain gauge-type transducer also has an accuracy of ±3%. Figure 10 shows a typical Kulite style transducer.

Pressure gauges employed by CUBRC are calibrated installed in the test article whenever possible. Calibration is carried out by subjecting each gauge to a traceable, steady pressure pulse lasting tens of milliseconds to duplicate what the gauge will experience during testing. This will occur over the range of expected pressures that the gauges will experience during testing.

Figure 9. Typical PCB Piezoelectric Pressure Transducer

Figure 10. Typical Kulite Piezoresistive Transducer

III. Model Design and Construction

The basic geometry for the HIFIRE-1 flight vehicle was given to CUBRC by AFRL and is shown in Figure 11 [Adamczak 2006]. The geometry consists of a blunt nose, 7° cone, flat cylinder section, a short 37° flare section and another flat cylinder aft end which ties into the booster. The CUBRC model represents a full-scale match of this configuration minus the slot that can be seen in the flare section. This slot will be present in the flight geometry to perform inlet mass capture optical measurements as they might relate to scramjet design. At this time it was deemed unnecessary to include this portion of the program in the CUBRC ground test. All model hardware components were machined on site at CUBRC and the as-built model is shown in Figure 12. This original configuration had a removable sharp nose and 37° degree flare section, both of which can be easily changed while the model is in the tunnel. Additional blunt noses of radius 2.5 and 5.0 millimeters were also manufactured. All the noses had considerations made for the inclusion of an electrical resistance cartage heater that would be used to heat the nose to predicted flight temperatures so that wall temperature effects could be studied. The temperature was monitored with several thermocouples embedded in the nose material and additionally the thin-film instrumentation installed in the cone was employed to specify the temperature profile down the length of the cone. CUBRC also constructed additional flare angles of 27°, 30°, and 33°. While the 37° flare angle was supported by numerical predictions, our correlations based on our earlier studies in shock wave/turbulent boundary layer interaction [Holden 1972, Holden 1970, Holden 1986] suggested that this angle was too large and that flare angles between 30° and 33° would achieve the required well-defined turbulent interaction region at the cylinder/flare junction. To assess the flare angle effectiveness during this phase of the program we employed high speed Schlieren video coupled with the results from earlier related studies to suggest the flare angle that should be employed on the flight vehicle. An installation diagram and photograph of the model installed in the LENS I facility is shown in Figure 13. A layout of the pressure and heat transfer instrumentation for this phase of testing can be seen in Figure 14.

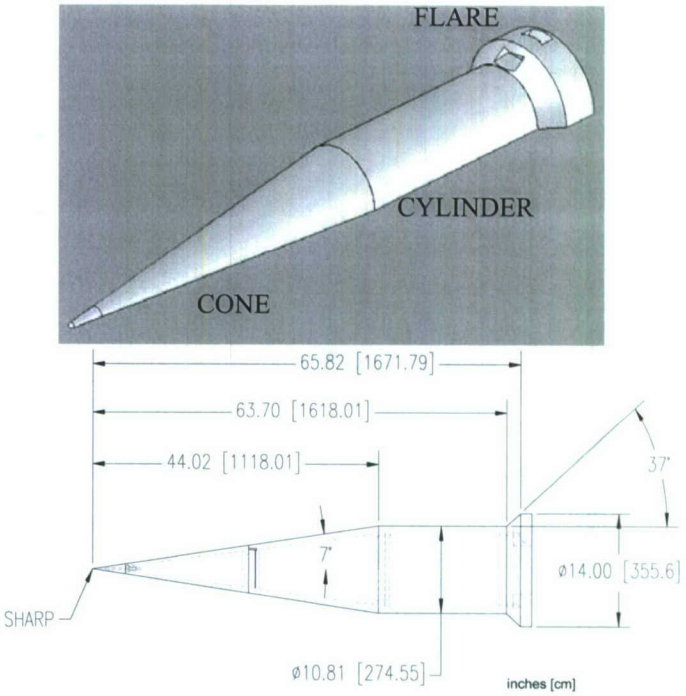

Figure 11. Basic FRESH FX-1 Flight Geometry

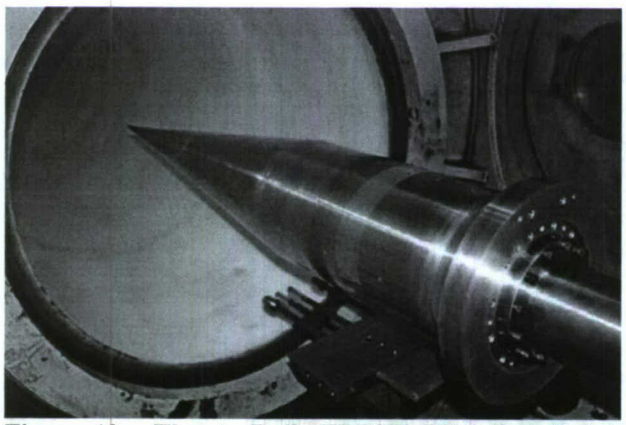

Figure 12. The As-Built FRESH FX-1 Installed in LENS I

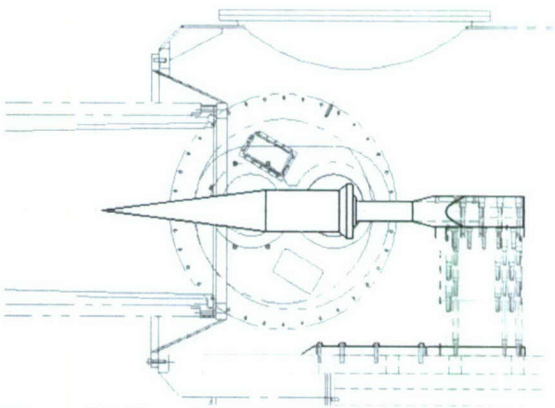

Figure 13. Drawing of Installed FRESH FX-1 Model in LENS I

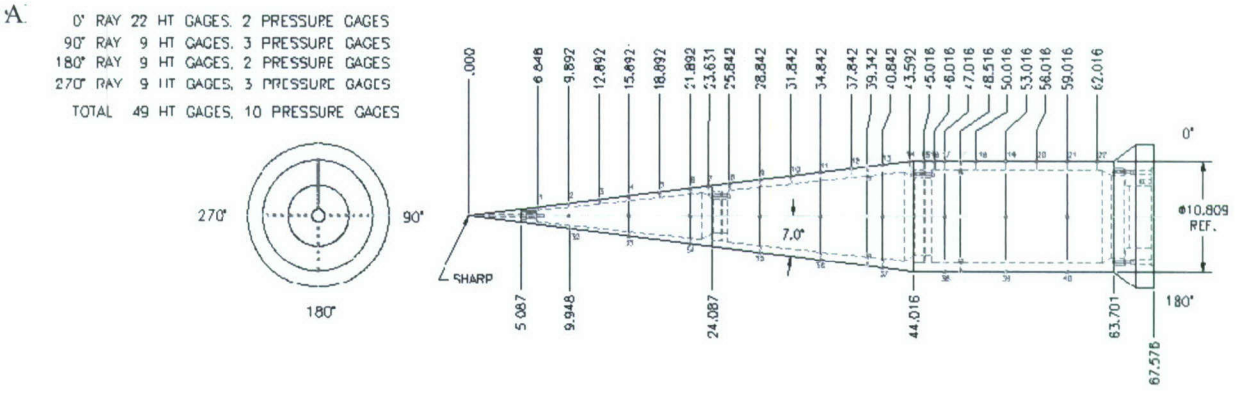

Figure 14. FRESH FX-1 Instrumentation Layout

IV. Selection of Freestream Conditions and Facility Flow Calibrations

The HIFIRE-1 flight trajectory as specified to CUBRC by AFRL is shown in Figures 15 and 16. [Kimmel 2006] Data will be taken over the entire flight from launch until such time as the vehicle or sensors fail during descent. The points where ideal transition conditions exist are marked with stars. How these points fall into LENS capabilities were shown in Figures 4 and 5. Each of the unique test conditions, shown in Table 1, that are to be run during the experimental program are first calibrated with test runs in the facility after being predicted computationally. The computational work allows for having to make fewer calibration runs at each condition and more importantly it adds greatly to the understanding of what is happening in the freestream at every condition. This will be important later when full model computations are performed. Basic instrumentation associated with the experimental calibration of the LENS facilities include: pressure sensors to monitor the initial driver and driven gas pressures and temperatures, thin-film resistance and piezoelectric pressure gauges installed at fixed locations on the driven tube to monitor the speed of the incident shock wave as it propagates down the tube, pressure sensors in the endwall region to measure the reflected shock reservoir pressure, a pressure sensor in the initially evacuated test section, and a survey rake installed in the test section to measure pitot pressure, static pressure and stagnation point heat transfer in the freestream. From these measurements and rake assembly, a comprehensive data set for each test condition was taken to calculate freestream conditions, core size, and flow uniformity of the freestream flow. A typical survey rake assembly is shown in Figure 17 together with the flowfield survey probes at the exit plane of the nozzle.

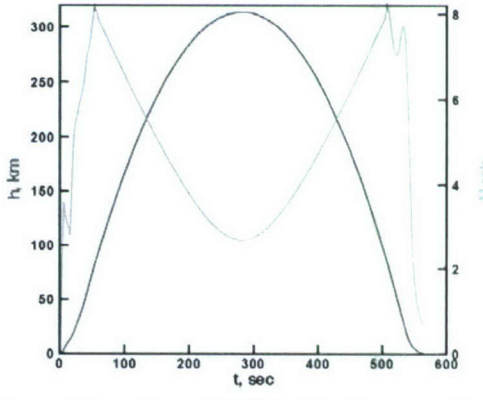

Figure 15. Overall Flight Trajectory of FRESH FX-1

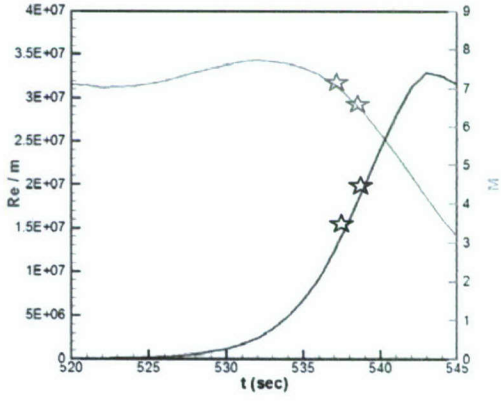

Figure 16. Detail Mach Number

High-frequency pressure instrumentation is typically used in the pitot probes. However, in regions where flows generate high thermal loads, we must employ thermal protection systems which lower the frequency response. Total temperature measurements are made in the lower enthalpy flows with shielded thermocouple probes while total heat transfer measurements are made with miniature thin-film or coaxial instrumentation placed in the stagnation region of a hemispherical nosetips.

Condition	Velocity (ft/sec)	Altitude (kft)	Temperature (°R)	Pressure (psia)	Density (slugs/ft^3)	Mach Number (-)	Reynolds Number (1/ft)
A	6,320	58.5	386	1.12	2.4E-4	6.58	5.3E+6
B	7,160	69.1	417	0.67	1.4E-04	7.16	3.1E+6

Table 1. Nominal Flight Conditions Duplicating Those Predicted from the Flight Trajectory

The first step in determining the test conditions in the LENS facility is to determine the conditions observed in the reservoir. This is accomplished via a combination of measurement and theory. The initial and final (reservoir) pressures are measured by a group of redundant pressure gauges in the endwall of the driven tube. The shock speed is also measured by a series of fast-response gauges down the length of the driven tube which react as the incident shock moves through the test gas. Using these pieces of information, the unique reservoir conditions may be computed from generalized equilibrium conditions and wave propagation theory after both the incident and the reflected shocks have passed through the test gas. The computation of the reservoir assumes full thermodynamic and chemical equilibrium at all points. This is a safe assumption, as the pressures and temperatures after the shocks are very large, thus making relaxation times exceptionally short. Relevant translational, rotational, and vibrational modes are considered in the energy of the molecules.

These results are now compared with the pre-calibration computational results. Figure 18 shows an example of the comparison of the Navier-Stokes and the measured pitot profile measurements for Mach 6.5, demonstrating the level of agreement obtained between CFD and experiment in the LENS programs. Pitot pressure is used as a measure of freestream accuracy for two primary reasons: (1) it is a directly measurable quantity, and (2) it is sensitive to the momentum in the flowfield. Hence, it is a good choice to judge the accuracy of the freestream specification. This is the same process CUBRC employs to prepare for any experimental program in the LENS facility.

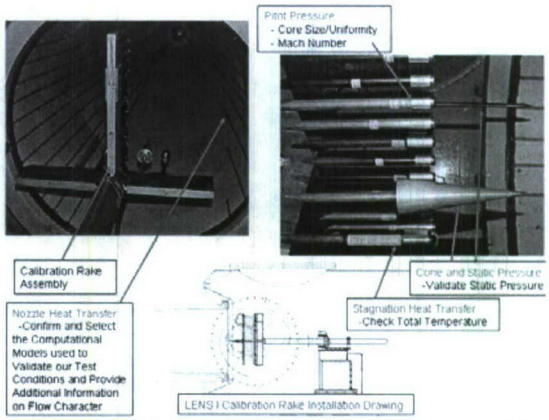

Figure 17. Photograph of Pitot Rake Assembly Mounted Inside Test Section of the LENS II Hypersonic Shock Tunnel

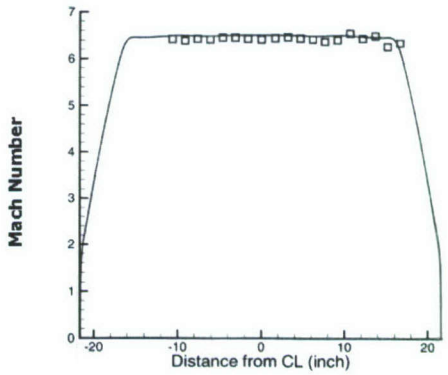

Figure 18. Comparison between Experimental and Computational Nozzle Profile

IV. The Experimental Studies

A. Nosetip Bluntness Effects on HIFIRE-1 Transition Results

The first part of the ground test program concentrated on specifying the nosetip bluntness that provides well-defined laminar, transitional, and turbulent regions on the cone section for each freestream condition including several angle of attack variations. Initial tests employing the sharp nosetip are shown for all heat transfer rays (0°, 90°, 180°, and 270°) in Figure 19. Here for test condition A (Mach Number of 6.5 and Reynolds Number of 5.0 million per foot) the turbulent region extends forward onto the removable nose section of the cone where no sensors exist. To confirm this assertion of turbulent flow the semi-empirical turbulent flow prediction method of Van Driest [Van Driest 1951] is employed and shows good agreement when compared with the experimental results for the length of the cone. The semi-empirical laminar prediction method of Cheng [Cheng 1961] is also shown with the experimental data always remaining well above this level by a factor of greater than 4. Computational results employing the DPLR code were done in parallel with the experimental program and will be discussed in Section V. Pressure results were also checked with simple Newtonian calculations and again show good agreement with the experimental results and confirm the specified freestream conditions.

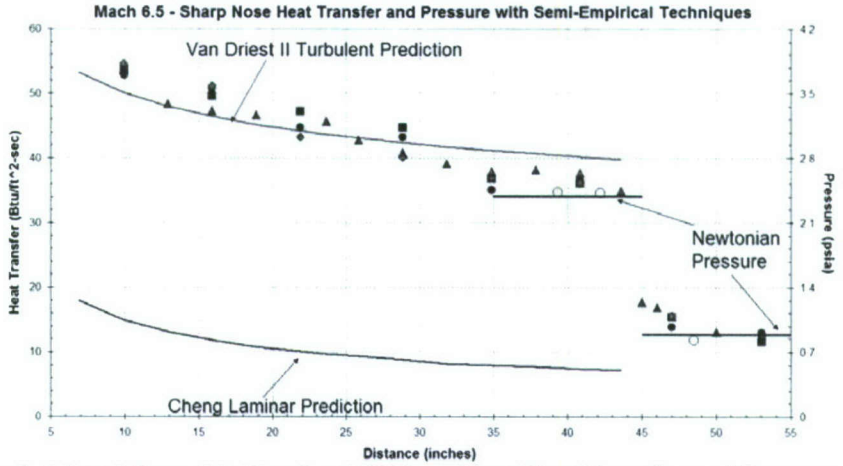

Figure 19. Mach 6.5 and Reynolds Number 5.0E6 per Foot Heat Transfer and Pressure Measurements with Sharp Nose Configuration Showing Transition Forward of First Sensor

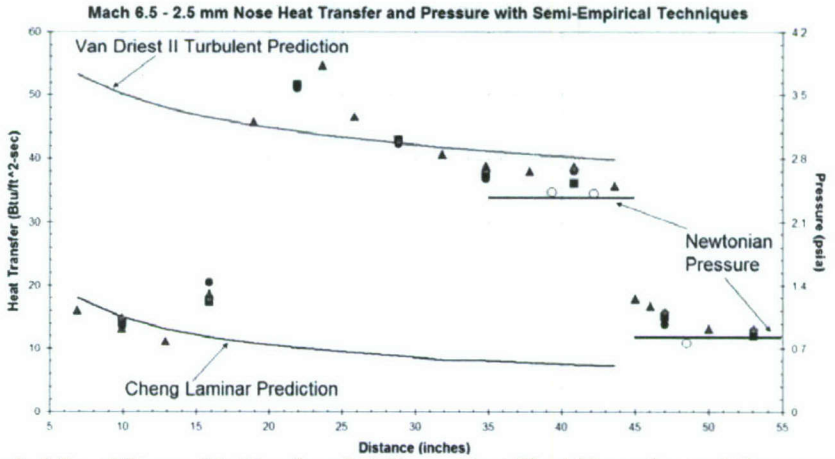

Figure 20. Mach 6.5 and Reynolds Number 5.0E6 per Foot Heat Transfer and Pressure Measurements with 2.5 mm Nose Configuration Showing Transition Delayed to 15 inches

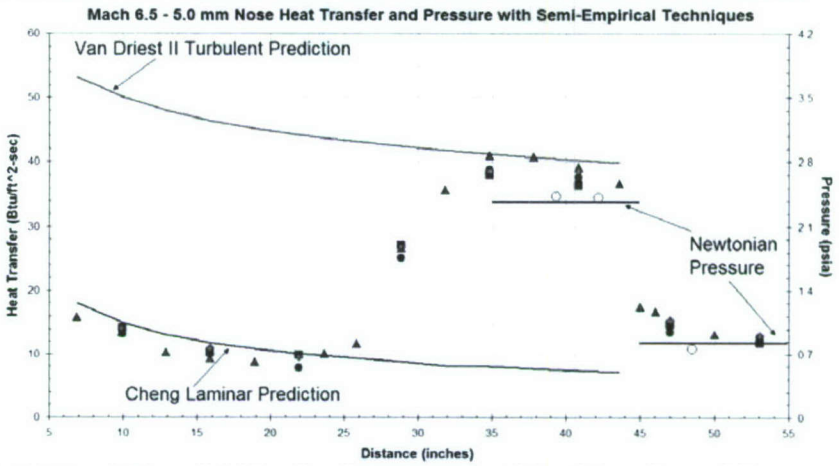

Figure 21. Mach 6.5 and Reynolds Number 5.0E6 per Foot Heat Transfer and Pressure Measurements with 5.0 mm Nose Configuration Showing Transition Delayed to 25 inches

The next experiment was conducted at the same freestream condition but the sharp nose was replaced by a blunt nose configuration of 2.5 millimeter radius. The heat transfer and pressure results are shown in Figure 20. The addition of the bluntness effects results in delaying the transition point to almost 15 inches. A well-defined laminar region now exists and agrees well with the Cheng prediction. There is a well-defined turbulent region that extends for 15 inches before the flow turns onto the cylinder section that agrees well with the Van Driest prediction. Also as with the sharp case there is good agreement between the pressure levels and the Newtonian prediction.

One additional bluntness, 5.0 millimeters, was also tested, the results of which are shown in Figure 21. Here while the laminar region is very well defined the fully turbulent region has been further delayed with increased bluntness and now occurs at 25 inches in front of the cone/cylinder junction.

The bluntness tests were then repeated for freestream condition B (Mach Number of 7.2 and Reynolds Number of 3.0 million per foot) to allow a decision on which bluntness produced the best defined flow characteristics on the nose. The sharp nose case was omitted at this condition due to the low level of confidence that a well-defined environment would be obtained based on the result from the earlier studies. Figure 22 shows the Mach 7.2 results for the 2.5 millimeter bluntness condition. Comparing this result to the one at Mach 6.5 we see that the transition point has moved downstream 3 inches. This result is encouraging in that the transition point does not move much due to the combination of Mach Number and Reynolds Number changes between the two conditions.

The 5.0 millimeter bluntness was also tested and the resulting data can be seen in Figure 23. The additional bluntness here moves the transition point another 2 inches downstream comparable to the results for the Mach 6.5 condition. Again, the transition location is similar to the results for the same bluntness at Mach 6.5.

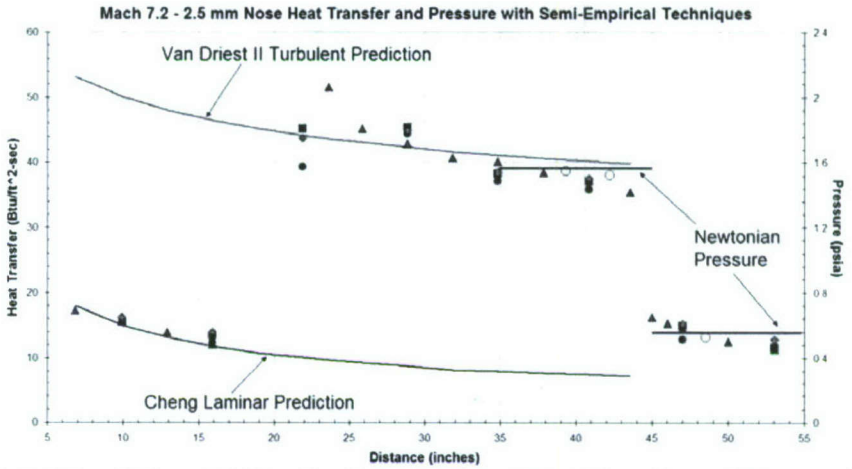

Figure 22. Mach 7.2 and Reynolds Number 3.0E6 per Foot Heat Transfer and Pressure Measurements with 2.5 mm Nose Configuration Showing Transition Delayed to 18 inches

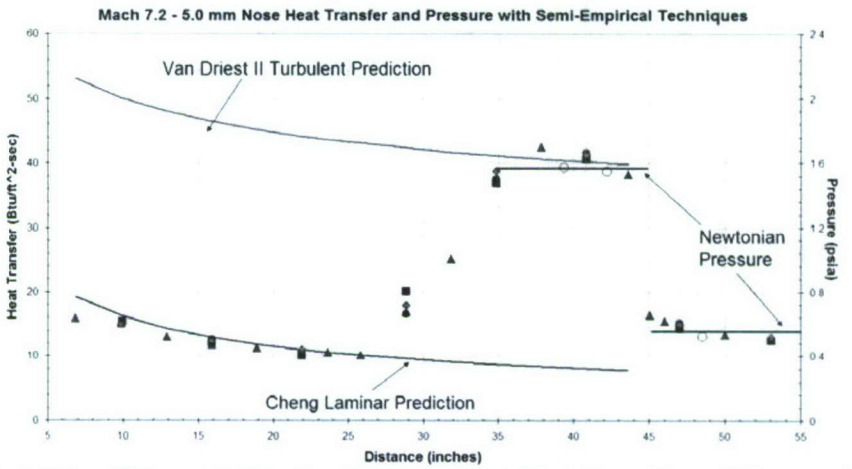

Figure 23. Mach 7.2 and Reynolds Number 3.0E6 per Foot Heat Transfer and Pressure Measurements with 5.0 mm Nose Configuration Showing Transition Delayed to 27 inches

These results at Mach 7.2 along with those at Mach 6.5 definitively show that the most well-defined flow configuration is produced with the 2.5 millimeter nose bluntness. While there are definable flow regions employing the 5.0 millimeter bluntness the turbulent region is too close to the cone/cylinder junction point considering there is the possibility that the transition point in flight could be further downstream. This consideration will elaborated on in the stability analysis discussion in Section V. Thus for zero degrees angle of attack the 2.5 millimeter bluntness case provides well-defined transition phenomena over the cone with a fully turbulent boundary layer ahead of the

flare at the three conditions specified on the predicted flight trajectory. In the next set of studies the angle of attack effects will be explored to see if the choice of nose bluntness is significantly affected.

B. Angle of Attack Effects on HIFIRE-1 Transition Results

In this series of experiments, heat transfer and pressure measurements were obtained for angles of attack of 1° and 5°. The flight program is designed to stay within angles of attack of 1° and 2°, but for the ground test the extreme angle of 5° was selected. These experiments were performed exclusively with the 2.5 millimeter radius nose to further validate the decision to employ this bluntness in flight. The heat transfer measurements for the two attitudes tested on the windward side of the model, shown in Figure 24, demonstrate that transition moves forward with increasing angle of attack until, at a model attitude of 5°, transition begins close to the nosetip and it is completed at the 15 inch axial station. These measurements were later repeated in the ground test program at both 1° and 5° angle of attack during the flare angle portion of the study and are also shown in Figure 24 and show excellent repeatability.

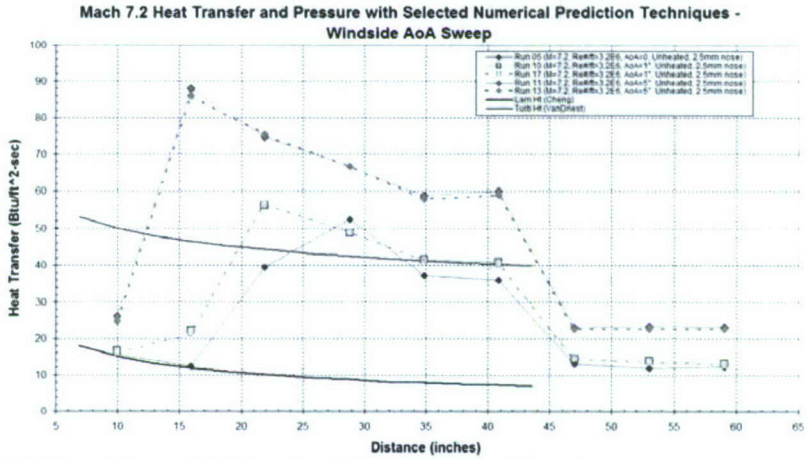

Figure 24. Mach 7.2 and Reynolds Number 3.0E6 per Foot Heat Transfer and Pressure Measurements with 2.5 mm Nose Showing Windward Angle of Attack Effects on Transition

Similar leeside measurements are shown in Figure 25. Transition characteristics vary only a little between model attitudes of 0° and 1° and show similar transition locations. However, at 5° incidence, the transition point has moved well forward on the cone resulting in turbulent heating over 35 inches of the cone. Additional leeside measurements were again made during the flare angle studies and similarly show excellent repeatability. This repeatability has been calculated to be within 5%.

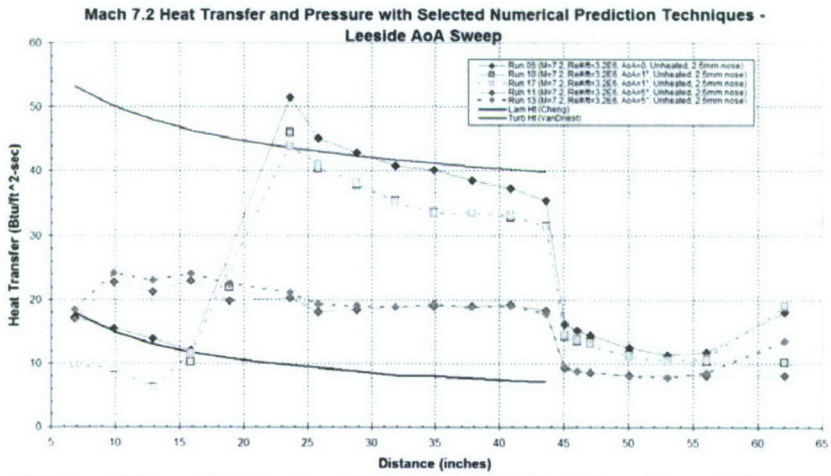

Figure 25. Mach 7.2 and Reynolds Number 3.0E6 per Foot Heat Transfer and Pressure Measurements with 2.5 mm Nose Showing Leeward Angle of Attack Effects on Transition

These results show that for the Mach Number, Reynolds Number, and angle of attack variations considered in this study the 2.5 millimeter nose bluntness is the best choice to achieve the goal of well-defined laminar, transitional, and turbulent regions during flight for code and ground test comparison and validation.

C. HIFIRE-1 Flare Angle Selection Studies

The second part of this phase of the ground test was focused on the selection of the proper flare angle for the flight test. As with the transition part of the flight experiment it is important to obtain flight data in a well-defined shock wave/boundary layer interaction region so that good comparisons with ground test and computational results may be made. This requires a fully turbulent boundary layer on the cylinder surface, definable separation and reattachment regions over the cylinder flare junction, and a measurable reattached flow region over the latter part of the flare to serve as a definable boundary condition for comparison purposes. Initially a flare angle of 37° was planned for the flight vehicle, but the flow characteristics needed to be experimentally tested to confirm this choice. During the ground test the flare was to remain uninstrumented so that changes could be quickly made while the model remained in the tunnel and this confirmation was to be carried out by CUBRC's high speed Schlieren video system. This system employs a copper vapor laser and a 10,000 frame per second Phantom version 7.0 camera that is synchronized to the laser pulses and is able to essentially "freeze" the flow phenomena.

Initial tests at condition B (Mach Number of 7.2 and Reynolds Number of 3.0E6 per foot) were performed with the 37° geometry. Results of these tests and a configuration diagram can be seen in Figure 26. The Schlieren photograph indicates that reattachment occurs close to or at the end of the flare so that there is not a significant attached region downstream of reattachment in which measurements could be made to define the downstream boundary conditions required to accurately evaluate the performance of the turbulence models employed in the prediction.

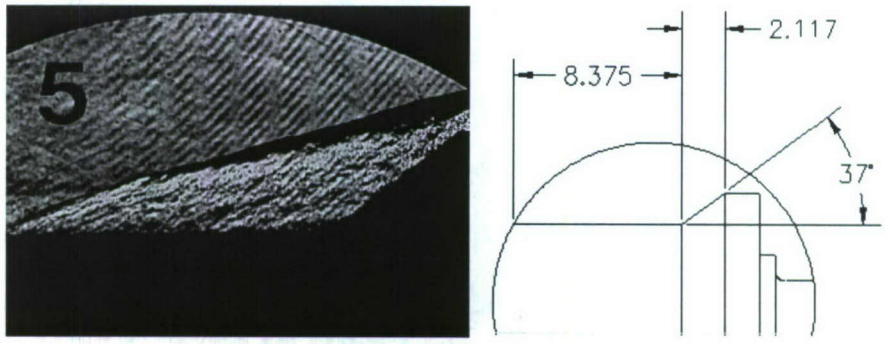

Figure 26. Schlieren Image of Flare Region at Mach 7.2 - 37° Flare Angle

Configuration studies at CUBRC prior to testing suggested that a 30° flare angle would be a good choice to obtain to desired flow characteristics, but due to angle of attack concerns lengthening the separated region on the leeside of the model it was decided to start with the flare angle at 27°. The Schlieren result and the configuration drawing from this test can be seen in Figure 27. In the Schlieren photo we see that the separated region is very small and the flare shock wave extends through the boundary layer almost to the cylinder/flare junction point. This flare case would not be satisfactory for the flight case.

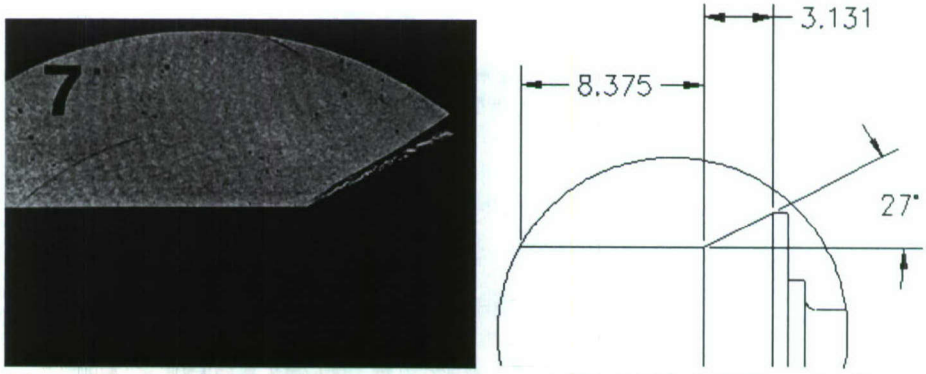

Figure 27. Schlieren Image of Flare Region at Mach 7.2 - 27° Flare Angle

The 27° degree flare was removed and replaced with a 30° flare angle and the model was retested at the same test conditions. The Schlieren image for this condition (Figure 28) now shows a slightly larger separated region and while this might be a good selection for angle of attack cases it remains too small for the required flight case geometry.

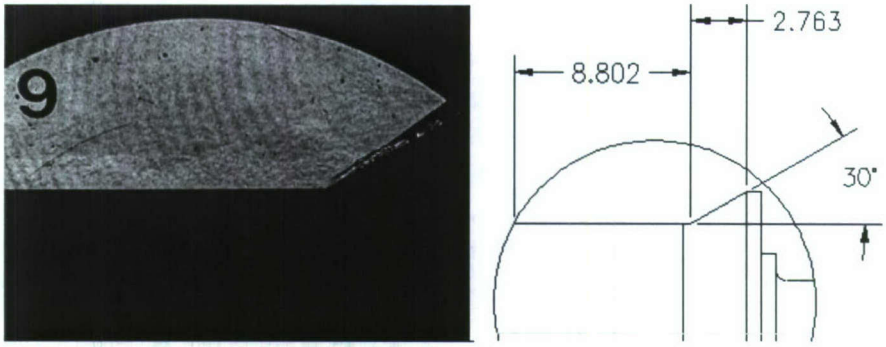

Figure 28. Schlieren Image of Flare Region at Mach 7.2 - 30° Flare Angle

The fourth and final flare angle of 33° was next tested at condition B and produced the Schlieren image shown in Figure 29. This flare angle produced a separated region that reattached about a two-thirds of the way up the flare producing a reattachment shock. These features indicate well-defined flow characteristics that can be expected to produce data downstream of the reattachment point that can be employed as a boundary condition for computationalists to validate turbulence models. Additional tests with this flare angle are now necessary to confirm well-defined characteristics for condition A (Mach 6.5) and for the angles of attack of 1° and 5°. Figure 30 shows the results for testing at condition A. This Schlieren shows a larger separated region when compared to condition B in Figure 29, but the reattachment point is still on the flare with a reattachment shock and room downstream for making boundary condition measurements. An angle of attack case is shown in Figure 31. Here we see that for the 1° case the windward flare is similarly well-defined.

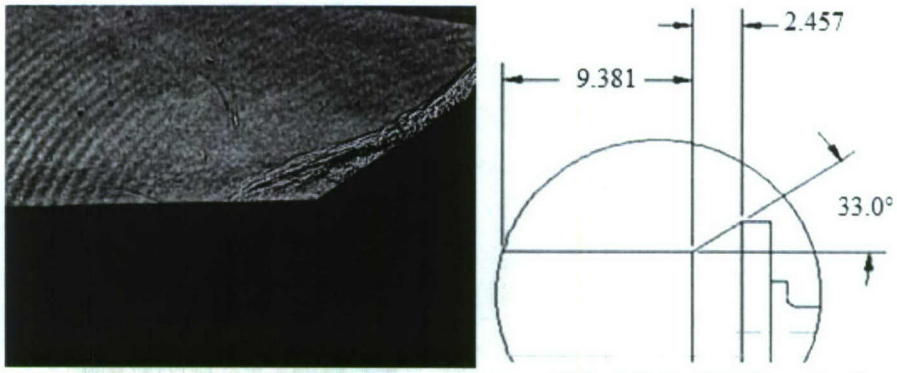

Figure 29. Schlieren Image of Flare Region at Mach 7.2 - 33° Flare Angle

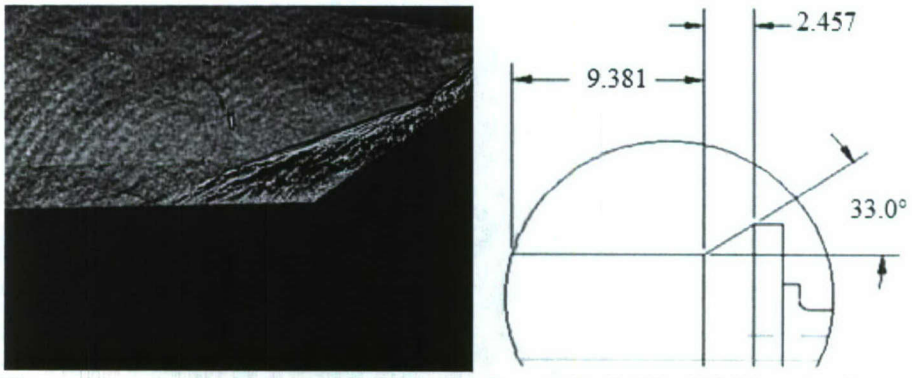

Figure 30. Schlieren Image pf Flare Region at Mach 6.5 - 33° Flare Angle

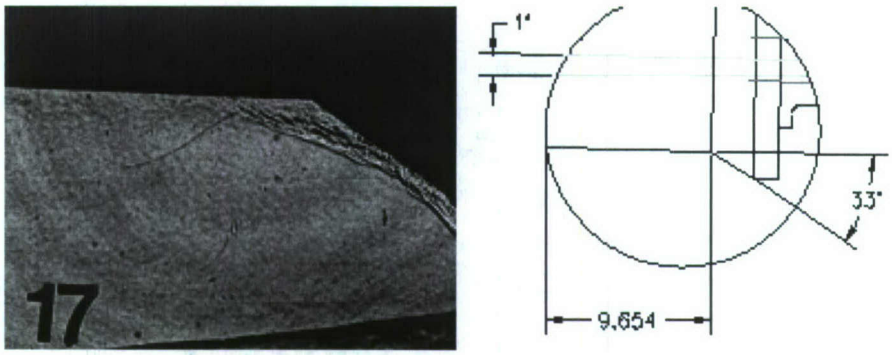

Figure 31. Schlieren Image of Flare Region at Mach 7.2 - 33° Flare Angle, 1° Angle of Attack

We finally conclude from the above studies that a configuration with the overall dimensions proposed by the U.S. Air Force but with a 2.5 mm nose radius for the cone and a 33° flare angle should provide a good configuration for the flight test studies. Also, we now have data on this configuration that will direct the placement of additional sensors for the second phase of the ground test program. This will be discussed in Section VI.

D. Wall Temperature Effects on Transition

An additional test with the final model configuration involved heating the model nose to investigate the effect of wall temperature on the transition location. Employing an electrical resistance heater installed in the removable nose tip we heated the nose and cone section to 800° R. We also monitored the temperature gradient up the nose section using the installed thin-film sensors that, in their simplest form, are resistance thermometers. The actual temperature gradient is shown in Figure 32. As shown the temperature starts at 800° F at the nose and returns to room temperature by 25 inches up the nose. These temperature values were sampled immediately prior to tunnel operation. The resulting data compared to the unheated model data is presented in Figure 33. Here it is shown for the conditions and temperatures tested that there is no measurable effect of wall temperature. This idea will be also explored from a stability viewpoint in Section V.

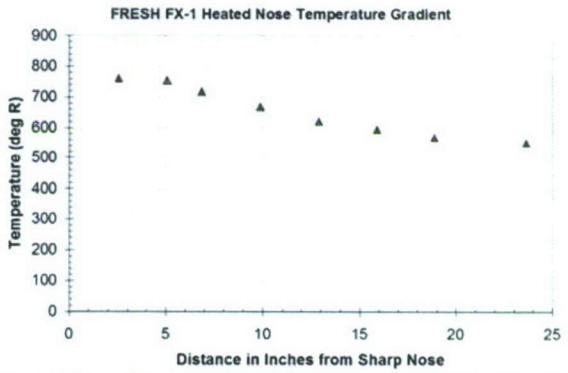

Figure 32. Pre-run Wall Temperature Gradient as Measured Thin-film Sensors

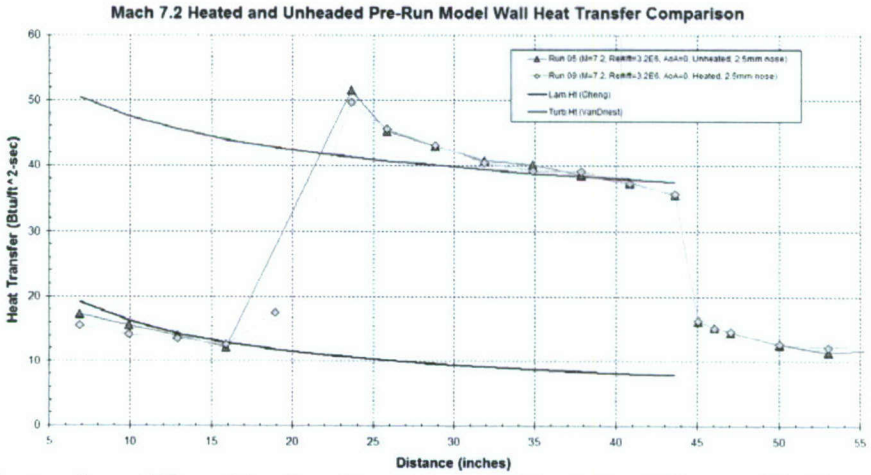

Figure 33. Comparison of Transition Location Between Unheated and Pre-run Heating of FRESH FX-1 Nose Region

V. Computational Results

A. DPLR Navier-Stokes Solver

All ground test studies in the LENS facilities are extensively calibrated and validated with numerical tools. The primary CFD tool used is the DPLR code provided by NASA Ames Research Center. DPLR is a multi-block, structured, finite-volume code that solves the reacting Navier-Stokes equations including finite rate chemistry and finite rate vibrational non-equilibrium effects. This code is based on the data-parallel line relaxation method [Wright 1998] and implements a modified (low dissipation) Steger-Warming flux splitting approach [MacCormack 1989] for the convection terms and central differencing for the diffusion terms. Finite rate vibrational relaxation is modeled via a simple harmonic oscillator vibrational degree of freedom [Candler 1995] using the Landau-Teller model [Landau 1936] Vibrational energy relaxation rates are computed by default from the semi-empirical expression due to Millikan and White [Millikan 1963], but rates from the work of Camac [Camac 1964] and Park, et al [Park 1994] are substituted for specific collisions where experimental data exists. Vibration-dissociation coupling is currently modeled using the *T-Tv* approach of Park [Park 1987] or with some preliminary implementation of CVDV coupling [Marrone 1963]. Transport properties are appropriately modeled in DPLR for high enthalpy flow [Palmer 2003, Palmer 2003] using the binary collision-integral based mixing rules from Gupta, et al [Gupta 1990]. Diffusion coefficients are modeled using the self-consistent effective binary diffusion (SCEBD) method [Ramshaw 1990]. Turbulence models available in the DPLR code currently include the Baldwin-Lomax 0-equation model [Baldwin 1978], the Spalart-Allmaras model 1-equation model [Spalart 1992], and the Shear Stress Transport (SST) 2-equation model [Menter 1994] each with corrections for compressibility effects [Brown 2002, Catris 1998]. Recent relevant capabilities of the DPLR code involve automated grid adaptation to improve solution quality [Saunders 2007].

B. STABL Tool Package/PSE-Chem Solver

The Stability and Transition Analysis for Hypersonic Boundary Layers (STABL) package [Johnson 2000, Johnson 2005, Johnson 2006] is a comprehensive suite of tools that features an integrated two-dimensional/axisymmetric chemically reacting laminar flow solver, equilibrium chemistry solver, parabolized stability solver, post-processor and various supporting tools and scripting wizards integrated into a single, intuitive, Perl-based GUI interface. The CFD and PSE solvers use MPI for efficient parallel processing. STABL is developed at the University of Minnesota (a combination of versions 2.4 and 2.6 were used for these analyses).

The PSE-Chem solver is a primary part of the STABL suite that solves the parabolized stability equations for two-dimensional or axisymmetric flow derived from the Navier-Stokes equations. The PSE equations are developed by modeling instantaneous flow variables with a mean and fluctuating component and subtracting the mean component from the resulting equation set. The result is a system of 2nd order partial differential equations for the disturbances, which are parabolized according to the method of Herbert [Herbert 1991] by assuming that the disturbances are composed of a fast-oscillatory wave part and a slowly-varying shape function. The ellipticity of the wave part is preserved while only the governing equation for the shape function is parabolized. Assuming that initial disturbances are small and making an assumption of "locally-parallel" flow at the starting plane allows sufficient simplification to generate an initial solution for the shape function and complex streamwise wavenumber. These initial solutions may then be marched downstream by integrating the parabolized stability equations.

The PSE analysis generates a prediction for the evolution of an initial disturbance as it moves downstream from its starting point through the mean flowfield. To predict the onset of transition, an experimental correlation is required. PSE-Chem uses the semi-empirical e^N correlation method

C. Comparisons of Laminar DPLR Solutions with Experimental Data

In parallel with the experimental testing CUBRC also performed computational analysis of the pressure and heating levels on both the cone and cylinder areas of the model. The laminar solutions were compared directly to the baseline laminar levels in the experiment prior to transition and were used to help guide the experimental program and add confirmation to the experimental freestream conditions and model data. These laminar solutions would later be imported directly into the STABL code and used in the stability calculations. Examples of laminar comparisons for both test conditions and bluntnesses can be seen in Figures 34-37. These comparisons show excellent agreement in the laminar flow region ahead of transition. These figures also show the excellent agreement

between the four rays of the model. The occasional rise in the data near the 60 inch portion of the plots is due to the flare induced separated region and changes from run to run as the flare angle is being modified.

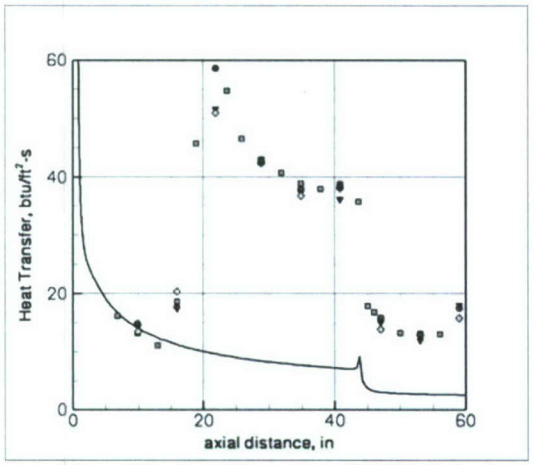

Figure 34. Mach 6.5 Laminar DPLR Solution of 2.5 mm Nose Case

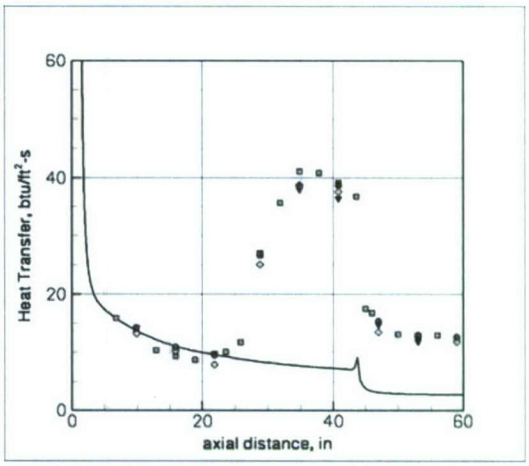

Figure 35. Mach 6.5 Laminar DPLR Solution of 5.0 mm Nose Case

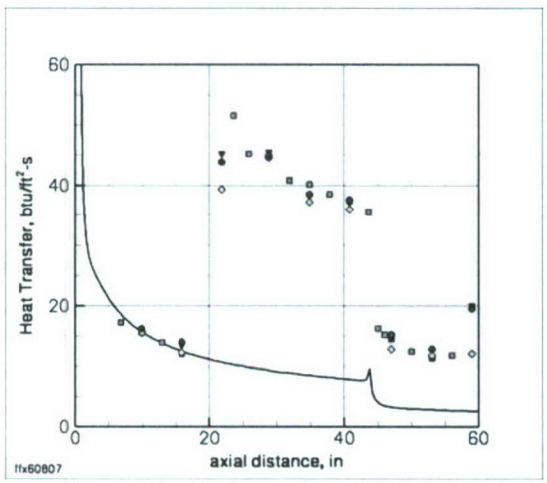

Figure 36. Mach 7.2 Laminar DPLR Solution of 2.5 mm Nose Case

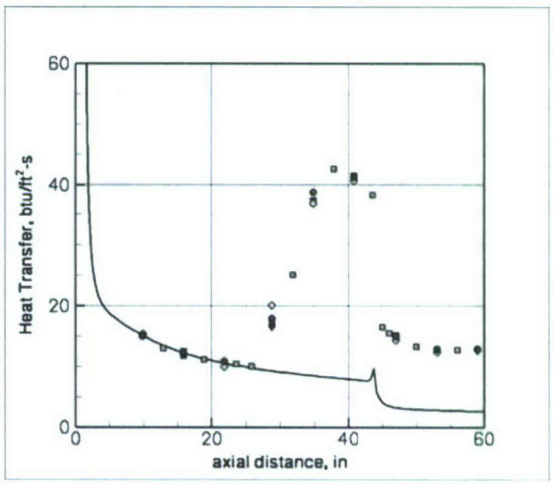

Figure 37. Mach 7.2 Laminar DPLR Solution of 5.0 mm Nose Case

D. Comparisons of Turbulent DPLR Solutions with Experimental Data

In contrast, the prediction of turbulent heating level with the various models that can be employed in the DPLR code are very significant depending on the selection of the compressibility correction as shown in Figures 38 and 39. The good agreement between prediction and measurement for the laminar flow anchors the calculations which clearly indicates significant differences between the turbulence models and the compressibility corrections selected. It is interesting to note that in fact the simplest model, Baldwin-Lomax [Baldwin 1978], appears to give predictions which more closely replicate the measurements, and also agree with the results of the semi-empirical Van Driest II prediction method (shown earlier). The RANS models give varying solutions of turbulent heating based at least partially on the correction for compressibility. Spalart-Allmaras model shows some sensitivity to freestream initialization while SST shows no sensitivity (as it should not). This is a surprising result for one would anticipate that turbulent attached flows over a simple model configuration at moderate hypersonic conditions should be accurately predicted by the current "sophisticated" techniques.

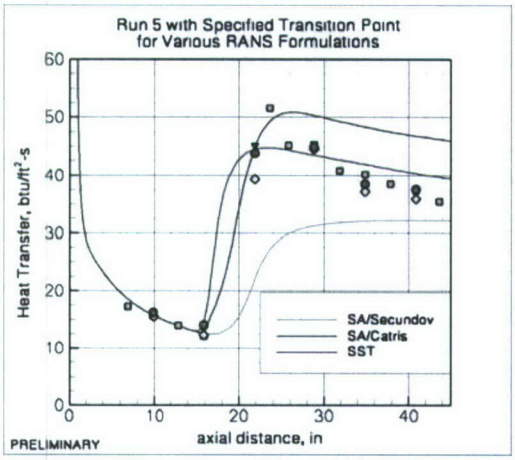

Figure 38. Examples of Several DPLR RANS Model Turbulent Predictions

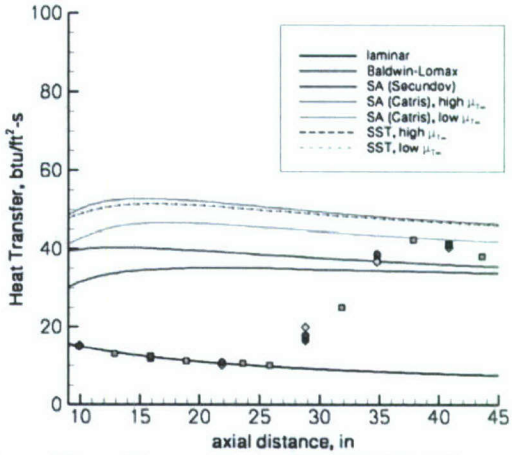

Figure 39. Comparison of RANS Model Compressibility Corrections

E. Employing the DPLR and STABL Codes to Estimate Transition Behavior on Flight Vehicle

The extrapolation of the ground test measurements to flight conditions using the STABL code provided an extremely valuable approach to employing ground test measurements to support the design of flight vehicles. In essence, the measurements made in the ground test environment are employed to calibrate the STABL code, which is then employed to determine the magnitude of the perturbation to transition position for N-factors which have been suggested from flight data. This process is illustrated in Figure 40, where the DPLR code is employed to predict the flow over the blunt cone configuration. The STABL Code solves the parabolized stability equations (PSE) for the growth of first and second mode instabilities by the integration of the disturbance using an e^n fit. Earlier studies have indicated that typical values for

N are 5.5 in the wind tunnel and 10 - 11 for flight vehicles. A stability map similar to that shown in Figure 40b is created, which then is employed to plot the n-factor axial distance envelope shown in Figure 40c. An N-factor for the ground test measurements is calculated based upon the measurements of insipient transition and employing flight N-factors of typically 10 one can extrapolate to determine the delay in transition expected for the flight case. Two examples of the extrapolation to flight using this approach are shown in Figure 41a and b for the Mach number 6.5 and 7.2 test conditions respectively. For the Mach 6.5 condition shown in Figure 41a, this extrapolation technique indicates that transition would move downstream on the cone by approximately 4.5 inches from its measured location at 15 inches. Clearly this is a small increment on the 45-inch cone and would support our conclusion that the model configuration proposed for the flight test was completely acceptable. A similar set of calculations at the 7.2 condition are shown in Figure 41b and again the predicted 10-inch movement of the transition point would not significantly influence our selection of the flight configuration. Additional results were obtained by Johnson at the University of Minnesota employing the same freestream conditions and model geometry [Johnson 2007]. These results are shown in Figure 42. Here an N-factor of 10 moves the transition point moves the transition point downstream by a factor of 5.5 inches; a similar result to the analysis performed by CUBRC.

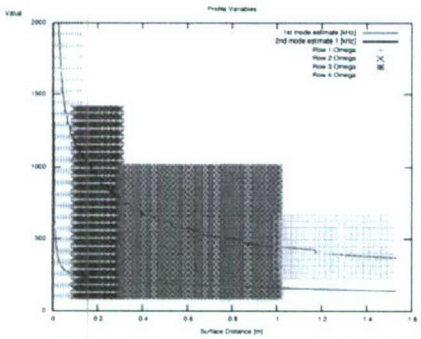

Figure 40a. Calculated Stability Modes

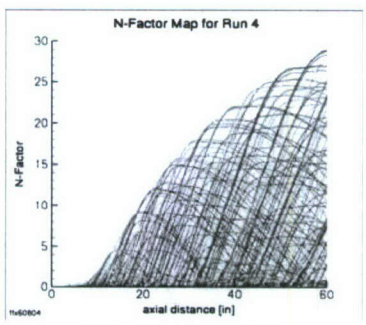

Figure 40b. Typical N-factor Map

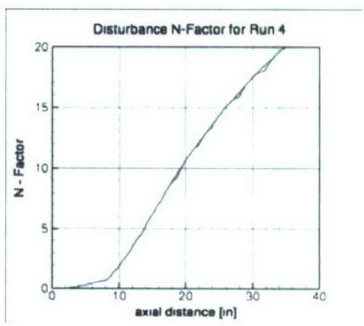

Figure 40c. Maximum N- Factors /Transition Boundary

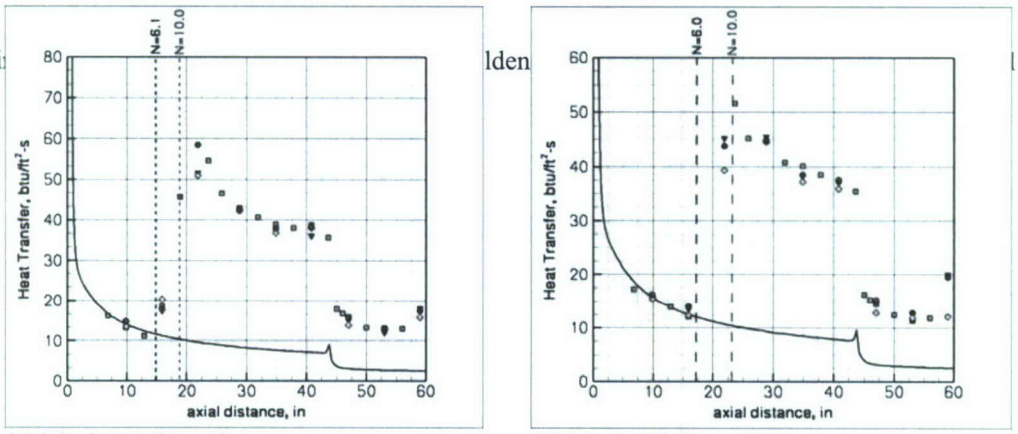

(a) Mach 6.5 (Run 4) (b) Mach 7.2 (Run 5)

- Assuming N_{FLIGHT} = 10 pushes transition back by ~ 4.5"
- This is still further forward than we measured with the larger nose radius (5.0 mm)
- The larger nose radius stayed turbulent beyond the expansion corner, so we conclude that the 2.5 mm radius should produce turbulent flow in the interaction region in flight

Figure 41. Predictions of the Downstream Movement of Transition from Ground Test to Flight

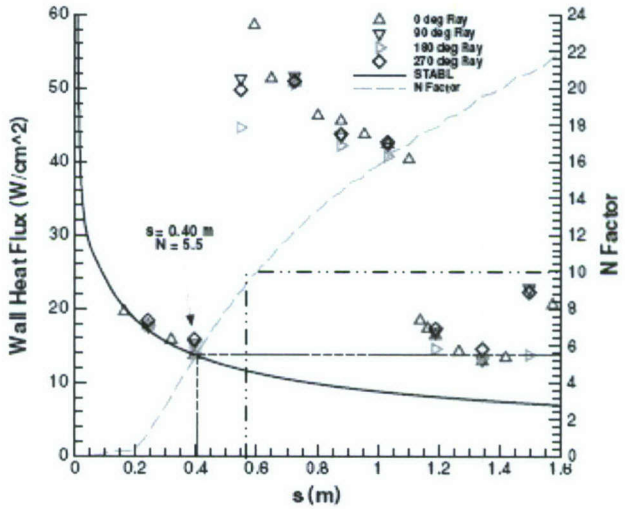

Figure 42. STABL Solution by Johnson Showing Similar Results for the HIFiRE-1 Mach 7.2 Case [Johnson 2007]

F. Comparing Wall Temperature Effects with STABL

During this series of experiments the STABL code was also employed to assess from a stability standpoint the effect of wall temperature. In one case the model is run at a pre-run temperature that is close to room temperature, and the other is run at a temperature approaching 800°R. The effect on the experimental results was discussed in section IV. The results of the analysis and experimental measurements are shown in Figure 42 a and b. Calculations shown in Figure 42a indicate that the stability boundary is only slightly affected by nosetip heating and assuming an N-factor of 10, the forward movement of transition as a result of heating would be less than 2 inches. A similar result can be inferred from the experimental data where the beginning and end of transition is virtually at the same point. This result would again support the selection of a nosetip bluntness of 2.5 mm for the conical section of the model which should prove to be sufficient in length to give well-defined data on the transition region in flight.

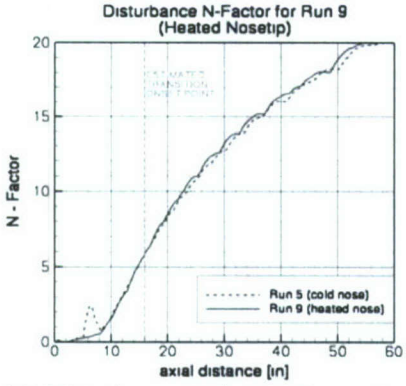

(a) Disturbance N-factor Comparison (Heated vs. Unheated Nosetip)

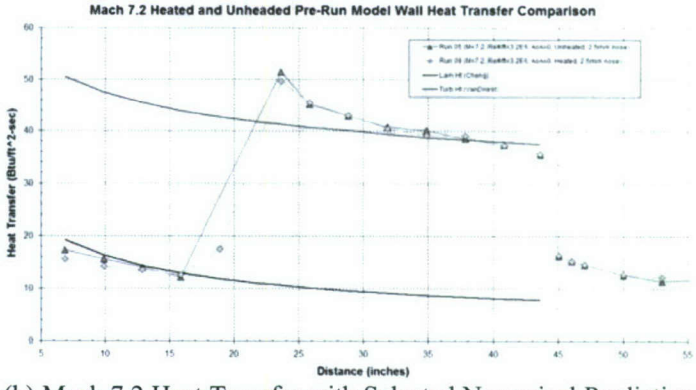

(b) Mach 7.2 Heat Transfer with Selected Numerical Prediction Techniques (Heated vs. Unheated Nosetip)

Result: Both experiment and stability computation show no significant influence on transition point from increased wall temperature

Figure 42. STABL and Experimental Measurements Comparing Heated versus Unheated

VI. Summary and Conclusions

Experimental studies have been conducted in hypersonic flows to provide measurements with which to evaluate and improve the modeling of turbulence phenomena associated with boundary layer transition and shock wave/boundary layer interaction. These studies were conducted at fully duplicated flight conditions in the LENS I tunnel employing full-scale models of the flight vehicle and components. The studies conducted for the AFOSR-sponsored HIFIRE-1 program were designed to aid in the selection of the configuration to be employed in the flight test program. Schlieren photographs and detailed heat transfer measurements were made to determine the characteristics of regions of boundary layer transition and shock wave/boundary layer interaction over the conical forebody and cylinder/flare section of the models. These measurements, together with numerical computations using the DPLR code, were employed to select a 2.5 mm nosetip radius and a 33° flare angle for the flight vehicle as well as verify that the overall length and geometry of the conical, cylindrical and flare sections of the model would provide valuable data in the flight test program. Flight vehicle geometry selections were further reinforced by stability calculations obtained employing the STABL code that predicted only several inches of down stream movement of the transition point in flight compared to the ground test. Measurements in turbulent flows in these programs gave rise to questions on the selection of the compressible turbulence models used in the numerical calculations. While the measurements were in excellent agreement with laminar DPLR solutions and semi-empirical methods developed over the past three decades, the measurements in fully turbulent regions of the HIFIRE-1 cone section were not well predicted using contemporary turbulence models in the DPLR prediction method. Additional studies in this area ongoing and will be reported at future AIAA meetings.

VII. Acknowledgments

This work was supported by the Air Force Office of Scientific Research under Grant FA9550-07-1-0150. The authors would like to acknowledge the support and guidance from Peter Erbland, Roger Kimmel, and David Adamczak of the Air Force Research Laboratories in Dayton Ohio and John Schmisseur of AFOSR.

VIII. References

1). AAEC Research Staff, "LENS Brochure", *Capabilities and Technologies*, Buffalo, NY 2004

2). Adamczak, David, Private Communication, 2006.

3). Holden, M.S., "Shock-Wave Turbulent Boundary Layer Interaction in Hypersonic Flow," AIAA Paper No. 72-74, Paper presented at the AIAA 10th Aerospace Sciences Meeting, San Diego, CA 17-19 January 1972.

4). Holden, M.S. and Moselle, J.R., "Theoretical and Experimental Studies of the Shock Wave-Boundary Layer Interaction on Compression Surfaces in Hypersonic Flow," Calspan Report No. AF-2410-A-1, October 1969, also ARL 70-0002, January 1970.

5). Holden, M.S., "A Review of Aerothermal Problems Associated with Hypersonic Flight," AIAA-86-0267, Paper presented at the AIAA 24th Aerospace Sciences Meeting, Reno, Nevada, 6-9 January 1986

6). Kimmel, Roger L., Gaitonde, Datta, Adamczak, David, "Fundamental RESearch in Hypersonics Flight eXperiments, FRESH FX-1 BLT & SBLI Experiments", PowerPoint Presentation, Dated June 6th, 2006.

7). Van Driest, E., R., "Turbulent Boundary Layer in Compressible Fluids", *Journal of the Aeronautical Sciences*, Volume 18, Pages 145-160, March 1951

8). Cheng, H.K.; Hall, Gordon; Gollian, T.C.; and Hertzberg, A., "Boundary-Layer Displacement and Leading-Edge Bluntness Effects in High-Temperature Hypersonic Flow", Journal of Aerospace Sciences, Volume 28, Pages 353-381, May 1961.

9). Wright, M.J.; Bose, D.; and Candler, G.V. "A Data Parallel Line Relaxation Method for the Navier-Stokes Equations". *AIAA Journal*. Vol 36, no 9. Pgs 1603 – 1609. Sept 1998.

10). MacCormack, R.W. and Candler, G.V. "The Solution of the Navier-Stokes Equations Using Gauss-Seidel Line Relaxation". *Computers and Fluids*. Vol 17, No 1. Pgs 135 – 150. 1989.

11). Candler, G.V. "Chemistry of External Flows". *Aerothermochemistry for Hypersonic Technology*: Von Karman Institute for Fluid Dynamics Lecture Series. VKI LS 1995-04.

12). Landau, L. and Teller, E. "Theory of Sound Dispersion". *Physikalische Zeitschrift der Sowjetunion*. Vol 10, no 34. 1936.

13). Millikan, R. and White, D. "Systematics of Vibrational Relaxation". *Journal of Chemical Physics*. Vol 39, no 12. Pgs 3209 – 3213. 1963.

14). Camac, M. "CO_2 Relaxation Processes in Shock Waves". *Fundamental Phenomena in Hypersonic Flow*. J.G. Hall Ed. Cornell University Press. Pgs 195 – 215, 1964.

15). Park, C.; Howe, J.T.; Jaffe, R.J.; and Candler, G.V. "Review of Chemical-Kinetic Problems of Future NASA Missions II: Mars Entries". *Journal of Thermophysics and Heat Transfer*. Vol 8, no 1. Pgs 9 – 23. 1994.

16). Park, Chul. "Assessment of Two-temperature Kinetic Model for Ionizing Air". AIAA Paper 87-1574. AIAA 22ND Thermophysics Conference. Honolulu, HI: 8-10 June 1987.

17). Marrone, P.V. and Treanor, C.E. "Chemical Relaxation with Preferential Dissociation from Excited Vibrational Levels". *The Physics of Fluids*, Vol 6, no 9. Pgs 1215 – 1221. September 1963.

18). Palmer, G.E. and Wright, M.J. "A Comparison of Methods to Compute High Temperature Gas Viscosity". *Journal of Thermophysics and Heat Transfer*. Vol 17, no 2. Pgs 232 – 239. 2003.

19). Palmer, G.E. and Wright, M.J. "A Comparison of Methods to Compute High Temperature Gas Thermal Conductivity". AIAA Paper 2003-3913. Jun 2003.

20). Gupta, R.; Yos, J.; Thompson, R.; and Lee, K. "A Review of Reaction Rates and Thermodynamic and Transport Properties for an 11-Species Air Model for Chemical and Thermal Nonequilibrium Calculations to 30000 K". NASA RP-1232. August 1990.

21). Ramshaw, J.D. "Self-consistent Effective Binary Diffusion in Multicomponent Gas Mixtures". *Journal of Non-Equilibrium Thermodynamics*. Vol 15, no 3. Pgs 295 – 300. 1990.

22). Baldwin, B.S. and Lomax, H. "Thin Layer Approximation and Algebraic Model for Separated Turbulent Flows". AIAA Paper 78-0257. Huntsville, AL: 1978.

23). Spalart, P.R. and Allmaras S.R. "A One-Equation Turbulence Model for Aerodynamic Flows". AIAA Paper 92-0439. 30TH Aerospace Sciences Meeting & Exhibit. Reno, NV: 6-9 Jan, 1992.

24). Menter, F.R. "Two-Equation Eddy-Viscosity Turbulence Models for Engineering Applications". *AIAA Journal*. Vol 32, no 8. Pgs 1598 – 1605. August 1994.

25). Brown, James. "Turbulence Model Validation for Hypersonic Flow". AIAA Paper 2002-3308. 8TH Thermophysics and Heat Transfer Conference. St. Paul, MN: 24 – 26 Jun 2002.

26). Catris S. and Aupoix B. "Improved Turbulence Models for Compressible Boundary Layers." AIAA Paper 98-2696. 2ND Theoretical Fluid Mechanics Meeting: Albuquerque, NM, June 1998.

27). Saunders, D.; Yoon, S.; and Wright, M. "An Approach to Shock Envelope Grid Tailoring and Its Effect on Reentry Vehicle Solutions," AIAA Paper 2007-0207. 45TH Aerospace Sciences Meeting & Exhibit. Reno, NV: 8-11 January 2007.

28). Johnson, Heath B. *Thermochemical Interactions in Hypersonic Boundary Layer Stability*. Ph.D. Thesis, University of Minnesota, Minneapolis, MN, 2000.

29). Johnson, H. and Candler, G. "Hypersonic Boundary Layer Stability Analysis Using PSE-Chem." AIAA Paper 2005-5023. 35TH AIAA Fluid Dynamics Conference and Exhibit, Toronto, ON. June 2005.

30). Johnson, H. and Candler, G. "Analysis of Laminar-Turbulent Transition in Hypersonic Flight Using PSE-Chem." AIAA Paper 2006-3057. 36TH AIAA Fluid Dynamics Conference and Exhibit, San Francisco, CA. 5 – 8 June 2006.

31). Herbert, T. "Boundary Layer Transition – Analysis and Prediction Revisited." AIAA Paper 91-0737. January, 1991.

32). Johnson, H.; Alba, C.; Candler, G.; MacLean, M.; Wadhams, T.; and Holden, M. "Boundary Layer Stability Analysis to Support the HiFiRE Transition Experiment". AIAA Paper 2007 – 0311. 45TH Aerospace Sciences Meeting & Exhibit. Reno, NV: 8-11 January 2007.